6th Workshop on Numerical Methods in Applied
Science and Engineering (NMASE 07)
Vall de Núria, 10 a 12 de enero de 2007

STRICT UPPER AND LOWER BOUNDS WITH ADAPTIVE REMESHING IN LIMIT STATE ANALYSIS

J. Muñoz[1*], A. Huerta[1], J. Bonet[2] and J. Peraire[3]

1: Dep. Applied Mathematics III, LaCàN
Univ. Poitècnica de Catalunya (UPC)
e-mail: j.munoz@upc.edu, web: http://www-lacan.upc.es

2: Civil and Computational Engineering Centre, School of Engineering
University of Wales, Swansea, UK

3: Department of Aeronautics and Astronautics
Massachusetts Institute of Technology, USA

Key words: limit state analysis, bounds, remeshing

Abstract. *By writing the limit state analysis as an optimisation problem, and after resorting to suitable discretisations of the stress and velocity field, we compute strict bounds of the load factor. The optimisation problem is posed as a Second Order Conic Program (SOCP), which can be solved very efficiently using specific algorithms for conic programming. Eventually, the optimum stress and velocity fields of the lower and upper bound problem are used to construct an error measure (elemental gap) employed in an adaptive remeshing strategy. This technique is combined with an additional adaptive nodal remeshing that is able to reproduce fan-type mesh patterns around points with discontinuous surface loads. We paticularise the resulting formulation for two-dimensional problems in plane strain, with Von Mises and Mohr-Coulomb plasticity. We demonstrate the effetiveness of the method with a set of numerical examples extracted from the literature.*

1 Introduction

Methods for the computation of loads estimates for limit state analysis have relayed traditionally in practitioners experience and a catalogue of solutions for simple academic cases. Although the latter are well founded in the lower and upper bound theorems of limit analysis [Che75, Chr96], it is still desirable to develop general methods that can be applied to a broader number of practical problems. In this regard, numerical methods for limit state analysis have gained increasing attention during the last decade (see for instance references [BZCF01, Chr96, KD03, LS02a, MM06]). This is partly due to the development of robust optimisation methods on which they strongly relay, and recent progress in the computation of strict bounds [Cir04, LS02a, MM06].

In the present paper, we compute strict upper and lower bounds of the load factor. This is achieved by constructing a set of purely static and kinematic interpolation spaces of the velocities and stresses, as described in [Cir04, DÓ5, Gut05]. The resulting discretisations of the lower bound problem have been also used in [LS02a, MM06], but differs from the upper bound discretisation given in [SK95, LS02b], where the admissible conditions are written as a function of the strains.

The solution of the constrained limit state problem is found resorting to Second Order Conic Programming (SOCP). We have used the general packages for conic programming SeDuMi [Stu99] and SDPT3 [TTT03], which are embedded in Matlab. We note that other specific programs for SOCP such as MOSEK [ApS05] have been recently used also in the context of limit analysis [MM06]. This is in contrast to the usual venue, where the bounds are computed resorting to Non-Linear Programming (NLP) [SK95, LS02a, LS02b, LSKH05, BZCF01, CA99, CP01, KD03]. However, the latter requires a two times differentiable boundary of the yield surface, i.e. no apex as in the Mohr-Coulomb or Drucker-Prager criteria. Several modifications or the linearised form of the usual yield surfaces are then necessary in order to solve the constraints with a non-linear programming technique [SK95, LS02b]. In contrast, SOCP does not require any modification of the usual admissibility plastic domains, as far as they can be written as a second order cone, which is the case in the usual plastic models such as Drucker-Prager, Mohr-Coulomb, Von Mises or Tresca. We restrict our study to 2D cases in plane strain in conjunction with Von Mises, Mohr-Coulomb or Tresca plasticity, although the formulation given here can be also written for plane stress problems [Cir04] or generalised to 3D problems.

Due to the presence of large areas that remain practically rigid, the need for adaptive remeshing strategy is a must. Since no *a priori* error estimates for limit state analysis exist, the usual approach is to use *a posteriori* techniques, such as non-zero strain rates and the proximity of the stresses to the yield surface [CP01], or alternatively the recovery of a Hessian matrix in order to provide an anisotropic error estimate [BZCF01, LSKH05]. We employ here an error estimate which is constructed from the combined solution of the lower and upper bound problem [Cir04, DÓ5, Gut05], and thus benefits from the dual structure of the limit analysis.

Additionally, in order to avoid the blocking of the lower bound when discontinuous loads are applied (as it is often the case in strip footings or foundation slabs), we combine the previous estimate with a strategy that remeshes according to the values of the velocities at the elemental edges. A similar criterion has been suggested in [LSKH05]. However, the strategy described here constructs radial remeshing patterns or fan-type meshes, which insert radial subdivisions only in the necessary directions. The need for fan-type patterns has been already pointed out in [Che75, LS02a, MM06, LSKH05]. In Appendix D we analyse the source of the blocking phenomena when no fans are used in the discretised problem, which interestingly, shows that the limit load factor of

the continuum problem is in fact governed by a local problem at the point of the load discontinuity.

We test and compare our formulation with a set of problems extracted from the literature [KHS05, LS02a, LS02b, LSKH05, MM06, ZBS02]. We show that the remeshing strategy described here is able to improve the bounds given so far for similar number of elements.

2 Duality and strict bounds in limit analysis

We henceforth consider a rigid-plastic body $\Omega \subset \mathbb{R}^2$, where the stresses $\boldsymbol{\sigma}$ are constrained to belonging to the domain

$$\mathcal{B} = \{\boldsymbol{\sigma} | f(\boldsymbol{\sigma}) \leq 0\}. \tag{1}$$

We require the following assumptions on the set $\mathcal{B}$:

- $\exists \epsilon > 0$, with $\sum_{i,j} |\sigma_{ij}| < \epsilon \Rightarrow \boldsymbol{\sigma} \in \mathcal{B}$ (the zero stress state belongs to $\mathcal{B}$).
- The set $\mathcal{B}$ is convex and closed.

Explicit expressions of the set $\mathcal{B}$ for Von Mises and Mohr-Coulmb plasticity are given in Appendix A.

The body is subjected to the body load $\lambda \boldsymbol{f}$ at the interior of Ω. In addition, the surface load $\lambda \boldsymbol{g}$ and homogeneous Dirichlet boundary conditions are applied at Γ_g and Γ_u, with $\Gamma_g \cap \Gamma_u = \emptyset$ and $\Gamma_g \cup \Gamma_u = \partial\Omega$. The objective of the limit state analysis is to determine the collapse load factor, denoted λ^*.

We note that due to the rigid-plastic assumption, and thus in contrast to elastic materials, no constitutive relation exists between the strain rate tensor[1] $\boldsymbol{\varepsilon}(\boldsymbol{u}) = \frac{1}{2}(\nabla \boldsymbol{u} + (\nabla \boldsymbol{u})^{\mathrm{T}})$ and the stress tensor $\boldsymbol{\sigma}$. Both variables are related through the associative plasticity rule $\boldsymbol{\varepsilon} = \gamma \partial f(\boldsymbol{\sigma}) / \partial \boldsymbol{\sigma}$, with γ the plastic multiplier. The assumption of associative plasticity is needed to formulate the lower and upper bound theorems, key ingredients of limit analysis that permit to compute load factor bounds and the stress and velocity fields at collapse. We henceforth denote by $\Sigma \ni \boldsymbol{\sigma}$ and $\mathcal{U} \ni \boldsymbol{u}$ the spaces for the stress and velocity field. The smooth requirements for Σ and $\mathcal{U}$ that guaranteee the existence of solutions can be found for instance in [Chr96].

2.1 Lower bound theorem

The lower bound theorem of limit analysis can be stated as follows [Che75]:

> *If for a given load factor $\tilde{\lambda}$ the stress field is such that (i) satisfies the stress boundary conditions, (ii) is in static equilibrium, and (iii) does not violate*

[1] We denote by $\boldsymbol{u}$ (or $\boldsymbol{v}$) and $\boldsymbol{\varepsilon}(\boldsymbol{u})$ *velociy* and strain *rates*, respectively.

the yield condition, the load factor is a lower bound of the collapse load, i.e. $\tilde{\lambda} \leq \lambda^*$.

The boundary equilibrium condition in (i) is given by $\boldsymbol{\sigma} \cdot \boldsymbol{n} = \lambda \boldsymbol{g}$ at Γ_g, with $\boldsymbol{n}$ the unit external normal, whereas the equilibrium condition in (ii) is equivalent to equalise the work rate of the external loads to the internal energy rate, which can expressed as follows:

$$a(\boldsymbol{\sigma}, \boldsymbol{v}) = \lambda \ell(\boldsymbol{v}), \ \forall \ \boldsymbol{v} \in \mathcal{U}. \tag{2}$$

The bilinear and linear forms $a(,)$ and $\ell()$ have the usual expressions:

$$\begin{aligned} a(\boldsymbol{\sigma}, \boldsymbol{v}) &= \int_\Omega \sigma : \boldsymbol{\varepsilon}(\boldsymbol{v}) dV, \\ \ell(\boldsymbol{v}) &= \int_\Omega \boldsymbol{f} \cdot \boldsymbol{v} dV + \int_{\Gamma_g} \boldsymbol{v} \cdot \boldsymbol{g} d\Gamma. \end{aligned} \tag{3}$$

It follows that, according to the lower bound theorem, the collapse load factor λ^* can be found by solving the following optimisation problem:

$$\lambda^* = \sup_{\substack{\lambda, \boldsymbol{\sigma} \in \mathcal{B} \\ a(\boldsymbol{\sigma}, \boldsymbol{v}) = \lambda \ell(\boldsymbol{v}), \ \forall \boldsymbol{v} \in \mathcal{U}}} \lambda. \tag{4}$$

From the expressions of $a(,)$ and $\ell()$ in (3), and after integrating by parts $a(,)$, we have that $a(\boldsymbol{\sigma}, \boldsymbol{v}) - \lambda \ell(\boldsymbol{v}) = -\int (\nabla \boldsymbol{\sigma} + \lambda \boldsymbol{f}) \cdot \boldsymbol{v} dV$ if the boundary equilibrium condition holds. Therefore, from the linearity of this expression in $\boldsymbol{v}$, we can write,

$$\inf_{\boldsymbol{v}} a(\boldsymbol{\sigma}, \boldsymbol{v}) - \lambda \ell(\boldsymbol{v}) = \begin{cases} 0 & \text{If } a(\boldsymbol{\sigma}, \boldsymbol{v}) = \lambda \ell(\boldsymbol{v}), \ \forall \boldsymbol{v} \in \mathcal{U} \\ -\infty & \text{Otherwise.} \end{cases} \tag{5}$$

Consequently, we can express λ^* in (4) as,

$$\lambda^* = \sup_{\lambda, \boldsymbol{\sigma} \in \mathcal{B}} \inf_{\boldsymbol{u}} \left(a(\boldsymbol{\sigma}, \boldsymbol{u}) + \lambda (1 - \ell(\boldsymbol{u})) \right) = \sup_{\boldsymbol{\sigma} \in \mathcal{B}} \inf_{\ell(\boldsymbol{u}) = 1} a(\boldsymbol{\sigma}, \boldsymbol{u}), \tag{6}$$

where the last identity follows from the fact that λ is a free variable.

2.2 Upper bound theorem

Let us introduce the internal rate of dissipation $D(\boldsymbol{u})$ as:

$$D(\boldsymbol{u}) = \sup_{\sigma \in \mathcal{B}} \int_\Omega \boldsymbol{\sigma} : \boldsymbol{\varepsilon}(\boldsymbol{u}) dV = \sup_{\sigma \in \mathcal{B}} a(\boldsymbol{\sigma}, \boldsymbol{u}). \tag{7}$$

From the associative plasticity rule, $D(\boldsymbol{u})$ may be expressed via the parameters in the yield function $f(\boldsymbol{\sigma})$, and an equivalent strain rate, $\varepsilon_{eq}(\boldsymbol{u})$, which also depends in the plasticity criteria considered. Expressions for $D(\boldsymbol{u})$ and $\varepsilon_{eq}(\boldsymbol{u})$ in Von Mises and 2D Mohr-Coulomb plasticity can be found in Appendix A.

With this definition at hand, the upper bound theorem of limit analysis can be stated as follows [Che75]:

> *Those loads determined by equating the external rate of work and the internal rate of dissipation in an assumed velocity field, which satisfies (i) the Dirichlet boundary conditions, and (ii) strain and velocity compatibility conditions, ($\boldsymbol{\varepsilon}(\boldsymbol{u}) = \gamma \partial f(\boldsymbol{\sigma})/\boldsymbol{\sigma}$ and $\boldsymbol{u} = 0$ at Γ_u), are not less than the collapse load.*

Therefore, according to the upper load theorem, the collapse load factor may be computed as,

$$\lambda^* = \inf_{D(\boldsymbol{u})=\lambda \ell(\boldsymbol{u})} \lambda = \inf_{u} \frac{D(\boldsymbol{u})}{\ell(\boldsymbol{u})} = \inf_{\ell(\boldsymbol{u})=1} D(\boldsymbol{u}) = \inf_{\ell(\boldsymbol{u})=1} \sup_{\boldsymbol{\sigma}\in\mathcal{B}} a(\boldsymbol{\sigma}, \boldsymbol{u}). \tag{8}$$

2.3 Duality and load factor bounds λ^{LB} and λ^{UB}

Both identities, (6) and (8), unveil the structure of limit state analysis: the optimum values $(\lambda^*, \boldsymbol{\sigma}^*, \boldsymbol{u}^*)$ are the saddle point of the bilinear form $a(\boldsymbol{\sigma}^*, \boldsymbol{u}^*) = \lambda^*$ in the domain $\mathcal{B} \times \mathcal{C}$, with $\mathcal{C} = \{\boldsymbol{u} \big| \ \ell(\boldsymbol{u}) = 1\}$. This fact permits to compute strict bounds of the collapse load factor λ^*. Assuming that the set $\mathcal{B} \ni \boldsymbol{\sigma}$ is convex, and since the objective function $a(\boldsymbol{\sigma}, \boldsymbol{u})$ and the constraint $\ell(\boldsymbol{u}) = 1$ are linear on their arguments (and therefore also convex), strong duality holds [BV04], which means the the optimum values λ^* in (6) and (8) are the same if they exist (see [Chr96] for existence conditions). Bounds of the collapse load factor may be then computed using the following relations:

$$\lambda^{LB} = a(\boldsymbol{\sigma}, \boldsymbol{u}^*) \leq \lambda^* = a(\boldsymbol{\sigma}^*, \boldsymbol{u}^*) \leq a(\boldsymbol{\sigma}^*, \boldsymbol{u}) = \lambda^{UB}. \tag{9}$$

These inequalities are satisfied for the spaces Σ and $\mathcal{U}$ describing the continuum fields $\boldsymbol{\sigma}$ and $\boldsymbol{u}$, respectively. We next introduce a set of discrete spaces Σ^h and $\mathcal{U}^h$ that preserve the validity of the two inequalities in (9).

3 Lower bound problem

3.1 Purely static spaces

Discrete spaces $\Sigma^{LB} \ni \boldsymbol{\sigma}^{LB}$ and $\mathcal{U}^{LB} \ni \boldsymbol{u}^{LB}$ that satisfy

$$\max_{\boldsymbol{\sigma}^{LB}\in\mathcal{B}^{LB}} \min_{\ell(\boldsymbol{u}^{LB})=1} a(\boldsymbol{\sigma}^{LB}, \boldsymbol{u}^{LB}) \leq \sup_{\boldsymbol{\sigma}\in\mathcal{B}} \inf_{\ell(\boldsymbol{u})=1} a(\boldsymbol{\sigma}, \boldsymbol{u}) \tag{10}$$

are termed *purely static spaces*. The admissible set of the discrete stresses, $\mathcal{B}^{LB}$, is determined below. Following a similar reasoning to (5), condition (10) is equivalent to

$$\max_{\lambda,\boldsymbol{\sigma}^{LB}\in\mathcal{B}^{LB}}\left(\lambda+\min_{\boldsymbol{u}^{LB}}a(\boldsymbol{\sigma}^{LB},\boldsymbol{u}^{LB})-\lambda\ell(\boldsymbol{u}^{LB})\right)\leq\sup_{\lambda,\boldsymbol{\sigma}\in\mathcal{B}}\left(\lambda+\inf_{\boldsymbol{u}}a(\boldsymbol{\sigma},\boldsymbol{u})-\lambda\ell(\boldsymbol{u})\right).$$

This relation is satisfied if the following two conditions hold:

$$a(\boldsymbol{\sigma}^{LB},\boldsymbol{u}^{LB})=\lambda\ell(\boldsymbol{u}^{LB})\;\forall\boldsymbol{u}^{LB}\in\mathcal{U}^{LB}\Rightarrow a(\boldsymbol{\sigma},\boldsymbol{u})=\lambda\ell(\boldsymbol{u})\;\forall\boldsymbol{u}\in\mathcal{U}, \tag{11a}$$

$$\mathcal{B}^{LB}\subseteq\mathcal{B}. \tag{11b}$$

A pair of spaces that satisfy these conditions can be constructed as follows. We discretise the domain with a triangulation $\mathcal{T}_h(\Omega)$ using $nele$ elements, and interpolate the stress and velocity fields as [Cir04],

- Σ^{LB}: Piecewise linear stress field interpolated from the nodal values $\boldsymbol{\sigma}^{n,e}$, $n=1,2,3; e=1,\ldots,nele$, with a set of complete Lagrangian functions I^n, i.e. $\sum_n I^n=1$. Discontinuity at each elemental boundary $\xi^e_{e'}$ (between elements e and e'), is permitted.
- $\mathcal{U}^{LB}$: Constant velocities at each element e. Additionally, a linear velocity field is introduced at each interior edge $\xi^e_{e'}$ and external edge ξ_e.

In addition, we also impose the stress admissibility condition to the nodal stress values, i.e. $\boldsymbol{\sigma}^{n,e}\in\mathcal{B}$. Since the interpolating functions are complete, and $\mathcal{B}$ is convex, we have that $\boldsymbol{\sigma}^{LB}\in\mathcal{B},\forall\boldsymbol{\sigma}^{LB}\in\Sigma^{LB}$. In fact $\boldsymbol{\sigma}^{LB}\in\mathcal{B}^{LB}\equiv\mathcal{B}$, and therefore (11b) holds.

The lower bound of the load factor, λ^{LB}, is computed recalling the lower bound theorem, in particular equation (4) in terms of the discrete spaces given above:

$$\lambda^{LB}=\max_{\substack{\lambda,\boldsymbol{\sigma}^{LB}\in\mathcal{B}^{LB}\\ a(\boldsymbol{\sigma}^{LB},\boldsymbol{v}^{LB})=\lambda\ell(\boldsymbol{v}^{LB}),\;\forall\boldsymbol{v}^{LB}\in\mathcal{U}^{LB}}}\lambda. \tag{12}$$

When using the discrete spaces $\boldsymbol{\sigma}^{LB}$ and $\boldsymbol{v}^{LB}$ in the expression of $a(,)$, and noting that $\boldsymbol{v}^{LB}$ is piecewise constant, the problem in (12) may be written as,

$$\lambda^{LB}\;=\;\max\lambda\quad s.t.\begin{cases}\nabla\boldsymbol{\sigma}^{LB}+\lambda\boldsymbol{f}=\boldsymbol{0}\\ \boldsymbol{\sigma}^{LB}\cdot\boldsymbol{n}=\lambda\boldsymbol{g}\text{ at }\Gamma_g\\ (\boldsymbol{\sigma}^{LB}_e-\boldsymbol{\sigma}^{LB}_{e'})\cdot\boldsymbol{n}^e_{e'}=\boldsymbol{0}\\ \boldsymbol{\sigma}^{LB}\in\mathcal{B}^{LB}\end{cases} \tag{13}$$

Since the equations in (13) are in fact the equilibrium equations of the continuum, condition (11a) holds. Consequently, since (11b) also holds, the spaces Σ^{LB} and $\mathcal{U}^{LB}$ are purely static.

It is shown in Appendix B that the optimisation problem in (13), for Von Mises or Mohr-Coulomb plasticity with $\phi = 0$, can be written in the following form:

$$\max \lambda$$
$$s.t. \left\{ \begin{array}{l} \left[\begin{array}{ccc} \mathbf{f} & \mathbf{0} & \mathbf{A}_M \\ \mathbf{g} & \mathbf{0} & \mathbf{N}^g_M \\ \mathbf{0} & \mathbf{0} & \mathbf{N}^e_{e'M} \\ \mathbf{0} & \mathbf{I} & \mathbf{0} \end{array} \right] \left\{ \begin{array}{c} \lambda \\ \mathbf{x}^{LB}_1 \\ \mathbf{x}^{LB}_{24} \end{array} \right\} = \left\{ \begin{array}{c} \mathbf{0} \\ \mathbf{0} \\ \mathbf{0} \\ \boldsymbol{b} \end{array} \right\} \\ \mathbf{x}^{LB}_4, \lambda \text{ free}, \mathbf{x}^{LB}_{13} \in \underbrace{\mathcal{L}^3 \times \ldots \times \mathcal{L}^3}_{3\times 3\times nele} \end{array} \right. ,$$

For Mohr-Coulomb plasticity with $\phi \neq 0$, the following expression is obtained instead:

$$\max \lambda$$
$$s.t. \left\{ \begin{array}{l} \left[\begin{array}{cc} \mathbf{f} & \mathbf{A}_M \\ \mathbf{g} & \mathbf{N}^g_M \\ \mathbf{0} & \mathbf{N}^e_{e'M} \end{array} \right] \left\{ \begin{array}{c} \lambda \\ \mathbf{x}^{LB}_{13} \end{array} \right\} = \left\{ \begin{array}{c} -\mathbf{d}_{AM} \\ -\mathbf{d}_{NM} \\ \mathbf{0} \end{array} \right\} \\ \lambda \text{ free}, \mathbf{x}^{LB}_{13} \in \underbrace{\mathcal{L}^3 \times \ldots \times \mathcal{L}^3}_{3\times 3\times nele} \end{array} \right. .$$

Explicit expressions of the matrices $\mathbf{A}_M$, $\mathbf{N}^g_M$, $\mathbf{N}^e_{e'M}$ and vectors $\mathbf{d}_{AM}$ and $\mathbf{d}_{NM}$ are also given in Appendix B. The variables $\mathbf{x}^{LB}$, which are a linear transformation of the stresses $\boldsymbol{\sigma}^{LB}$, have been introduced in order to express the yield surface as a product of second order cones (also named Lorentz or quadratic) $\mathcal{L}^3 = \{\mathbf{x} \in \mathbb{R}^3 \big| x_1 \geq \sqrt{x_2^2 + x_3^2}\}$.

The resulting optimisation problem is highly sparse and have the standard form of a SOCP. Specific techniques for such problems have been developed recently, and in particular, we have used SeDuMi [Stu99] and SDPT3 [TTT03] with satisfactory results, as the numerical examples in Section 6 show. As a general remark, we comment that while SeDuMi is faster than SDPT3, the latter has demonstrated, in our examples, to be more robust than the former.

4 Upper bound problem

4.1 Purely kinematic spaces

Discrete spaces $\Sigma^{UB} \ni \boldsymbol{\sigma}^{UB}$ and $\mathcal{U}^{UB} \ni \boldsymbol{u}^{UB}$ where the relation

$$\sup_{\boldsymbol{\sigma}\in\mathcal{B}} a(\boldsymbol{\sigma},\boldsymbol{u}) \leq \max_{\boldsymbol{\sigma}^{UB}\in\mathcal{B}^{UB}} a(\boldsymbol{\sigma}^{UB},\boldsymbol{u}^{UB}) \tag{14}$$

holds are termed *purely kinematic spaces*. Such discrete spaces are described next, and their kinematic nature demonstrated.

We resort to the same triangulation $\mathcal{T}_h(\Omega)$ employed in the lower problem, whereas the discrete stress and velocity fields are given by [Cir04]:

- Σ^{UB}: A piecewise constant stress field $\boldsymbol{\sigma}^{UB}$ at each element e is considered, which is in general discontinuous at the element edges. In addition, we introduce a tension field $\boldsymbol{t}^{UB}$ defined at each internal edge $\xi^e_{e'}$.
- $\mathcal{U}^{UB}$: Piecewise linear velocities at each element e, which are also discontinuous at the element edges.

The computation of the upper bound is not computed using the upper bound theorem, but resorting also to equation (4), in conjunction with discrete spaces that guarantee that relation (14) is not violated. The upper bound load factor λ^{UB} is then the solution of the following optimisation problem:

$$\lambda^{UB} = \max_{\substack{\lambda,\boldsymbol{\sigma}^{UB}\in\mathcal{B}^{UB} \\ a(\boldsymbol{\sigma}^{UB},\boldsymbol{v}^{UB})=\lambda\ell(\boldsymbol{v}^{UB}),\ \forall\boldsymbol{v}^{UB}\in\mathcal{U}^{UB}}} \lambda. \tag{15}$$

In order to proof the purely kinematic nature of the spaces Σ^{UB} and $\mathcal{U}^{UB}$ defined above, we first note that from the linearity of the stress field employed Σ^{UB}, which is constant, the computation of the maximum

$$\max_{\boldsymbol{\sigma}^{UB}\in\mathcal{B}^{UB}} a(\boldsymbol{\sigma}^{UB},\boldsymbol{u}^{UB})$$

is reached for an element-wise constant strain rate field. Since the velocity field $\mathcal{U}^{UB}$ is linear at each element interior, the maximum can be computed exactly if $\mathcal{B}^{UB}\equiv\mathcal{B}$, or at least exceeded if $\mathcal{B}^{UB}\supseteq\mathcal{B}$. In our case we resort to the latter case and use a discrete set of admissible stresses $\mathcal{B}^{UB}$ that satisfies the relation

$$\mathcal{B}^{UB}\supseteq\mathcal{B}. \tag{16}$$

This can be ensured by imposing $\boldsymbol{\sigma}^{UB}\in\mathcal{B}$ at the interior of the triangles, and imposing equivalent admissibility conditions to the tension field $\boldsymbol{t}^{UB}$. The edge tensions can be interpreted as the projection of a stress field at the edges. The definition of the admissibility set of $\boldsymbol{t}^{UB}$, denoted by $\mathcal{B}^{UB}_t$, parallels that of the the set $\mathcal{B}$, and therefore depends on the plastic model considered. In Von Mises plasticity, we interpret $\boldsymbol{t}^{UB}$ as the projection of an admissible pure shear stress σ_{xy}, and therefore we require,

$$\mathcal{B}_t^{UB} = \{\boldsymbol{t}^{UB} \big|\ |t_T^{UB}| \leq \sigma_Y/\sqrt{3}\} \tag{17}$$

whereas in Mohr-Coulomb plasticity we choose:

$$\mathcal{B}_t^{UB} = \{\boldsymbol{t}^{UB} \big|\ |t_T| \leq c + t_N \tan\phi\}, \tag{18}$$

where t_T and t_N are the tangent and normal components of $\boldsymbol{t}^{UB}$ with respect to the orientation of the edge $\xi_{e'}^e$. It can be verified that for both cases, $\boldsymbol{\sigma}^{UB} \in \mathcal{B} \Rightarrow \boldsymbol{t}^{UB} \in \mathcal{B}_t^{UB}$, and hence $\mathcal{B}_t^{UB} \supseteq \mathcal{B}$. Therefore, (16) is satisfied, and the spaces Σ^{UB} and $\mathcal{U}^{UB}$ are purely kinematic.

In Appendix C we turn the upper bound optimisation problem in (15) into a standard SOCP, which are explicitly given in equation (42). We just mention that, like in the lower bound problem, we transform the elemental stress $\boldsymbol{\sigma}^{UB}$ into a set of elemental variables $\mathbf{x}^{UB}$ that allow us to recast the membership constraints $\boldsymbol{\sigma}^{UB} \in \mathcal{B}$ in the form $\mathbf{x}^{UB} \in \underbrace{\mathcal{L}^3 \times \ldots \times \mathcal{L}^3}_{nele}$.

5 Mesh adaptivity

In order to capture the localisation of the strains and stresses that characterise the solution of limit state analysis, the design of an efficient mesh adaptivity strategy is highly desirable. We describe first an elemental error estimate which is a good candidate for a remeshing technique. Despite its good performance in general problems, it is not able to construct fan-type remeshing patterns, which a required in certain problems. For this reason second remeshing strategy is also constructed which has been numerically proven to converge to the optimal solution.

5.1 Elemental error estimate

We define the elemental gap as Δ_h^e,

$$\begin{aligned}\Delta_h^e &= D^e(\boldsymbol{u}^{UB}) \\ &\quad - \underbrace{\left(\int_{\Omega^e} (-\nabla\cdot\boldsymbol{\sigma}^{LB})\cdot\boldsymbol{u}^{UB} dV + \int_{\partial\Omega^e} (\boldsymbol{n}^e\cdot\boldsymbol{\sigma}^{LB})\cdot\boldsymbol{u}^{UB} dS\right)}_{l^e(\boldsymbol{u}^{UB})}.\end{aligned} \tag{19}$$

The first term is the elemental work dissipation, which is computed in a similar manner to the global work dissipation detailed in Appendix A, equations (21) and (25), but integrating over the elemental domain Ω^e. More specifically, for Von Mises plasticity, $D^e(\boldsymbol{u}^{UB}) = \int_{\Omega^e} \sigma_Y \varepsilon_{eq}(\boldsymbol{u}^{UB}) dV$, and in Mohr-Coulomb plasticity, $D^e(\boldsymbol{u}^{UB}) = \int_{\Omega^e} 2c\cos\phi\varepsilon_{eq}(\boldsymbol{u}^{UB}) dV$, where the expressions of $\varepsilon_{eq}(\boldsymbol{u}^{UB})$ for each plastic model are also given in (21) and (25).

It is shown in [Cir04] that (i) $\Delta_h^e \geq 0$ and (ii) $\sum_e \Delta_h^e \to \lambda^{UB} - \lambda^{LB}$ as $h \to 0$, and thus, Δ_h^e it is a good candidate for an error estimate. Accordingly, our remeshing strategy consists in remeshing those elements whose elemental bound gap is larger than a given threshold factor η_Δ of the larger elemental bound gap, i.e. such that

$$\Delta_h^e > \eta_\Delta \max_e \Delta_h^e.$$

The selected elements are remeshed according to the pattern given in Figure 1a.

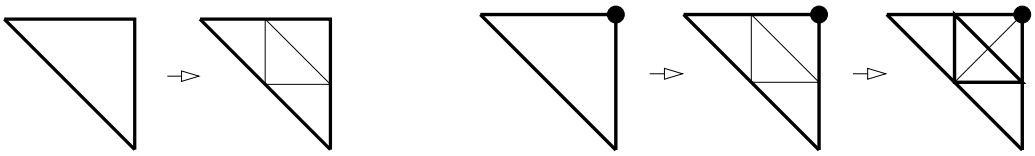

(a) (b)

Figure 1: Remeshing pattern for (a) Elemental remeshing, and (b) radial remeshing for a given edge velocity.

5.2 Radial remeshing strategy

For problems with discontinuous Neumann conditions, such as the strip footing problem analysed in Section 6.1, it has been reported the need to use meshes with a fan-type pattern [LS02a, MM06]. Regarding the elemental gap defined in (19), it has been verified numerically that in such cases, although $\Delta_h^e \to 0$, we don't have the desired relation $(\lambda^{UB} - \lambda^{LB}) \to 0$. Moreover, as it is explained in the Appendix D, the only active constraints are those at the edges of the elements connected to the point where the load is discontinuous. Since the edge velocities are conjugated to the edge equilibrium equations, the following additional strategy is employed: elements that have nodes with edge velocities larger than a given relative factor η_u, $0 < \eta_u < 1$, are subdivided according to the pattern in Figure 1b. In other words, if a node i belonging to element e satisfies

$$\|\boldsymbol{u}^{i,e}\| > \eta_u \max_{k,l} \|\boldsymbol{u}^{k,l}\| \quad k = 1, 2, 3; l = 1 \ldots nele,$$

this element is subdivided at node i. This strategy is applied after the elemental remeshing described in the previous section is performed. We note that additional subdivisions may be necessary in order to generate a conforming mesh, as indicated in Figure 1b. This strategy is capable of generate fan-type meshes. Furthermore, since the edge nodal velocities affect just to two elements in 2D, the radial subdivision is applied to certain directions only.

6 Numerical examples

6.1 Rigid strip footing

This problem has been widely studied [LS02a, LS02b, Gut05, DÓ5, LZC04, LSKH05, KHS05, MM06]. The load of a flexible strip footing is applied on an assumed weightless soil (see Figure 2a). For a purely cohesive material ($\phi = 0°$) in plane strain, the analytical solution is given by $\lambda/c = (2+\pi)c$ [Che75]. We show that the mesh strategy explained in Section 5.2 manages to unblock the lower bound due to the introduction of a fan-type mesh around the point with the surface load discontinuity. In order to illustrate the effect of the remeshing strategy, we have plotted in Figure 3 the linear velocities of the edges and the constant velocities of the body element. We recall that these are conjugate to the body equilibrium equations, $\nabla \cdot \boldsymbol{\sigma} + \lambda \boldsymbol{f} = \mathbf{0}$, and the edge equilibrium equations, $(\boldsymbol{\sigma}^e - \boldsymbol{\sigma}^{e'}) \cdot \boldsymbol{n}^e_{e'} = \mathbf{0}$, for an edge connecting elements e and e'. It can be deduced from the graphs that the only active constraints are the latter edge equilibrium relations (the body velocities are practically zero). As it can be observed from the evolutions of the bounds in Figure 2b, the radial subdivision of the elements that have larger velocities at the edges manages to unblock the lower bound and converges to the exact values. Figure 4 shows the resulting mesh after employing 4 elemental and radial remeshing loops. Interestingly, it is shown in Appendix D that the limit load factor for this problem can be obtained by just analysing the point with the load discontinuity, which in fact requires a minimal number of elements. Indeed, the local analysis with 12 elements leads to a better lower bound (5.1165) than the analysis of the whole domain with more than 3000 elements (5.1148).

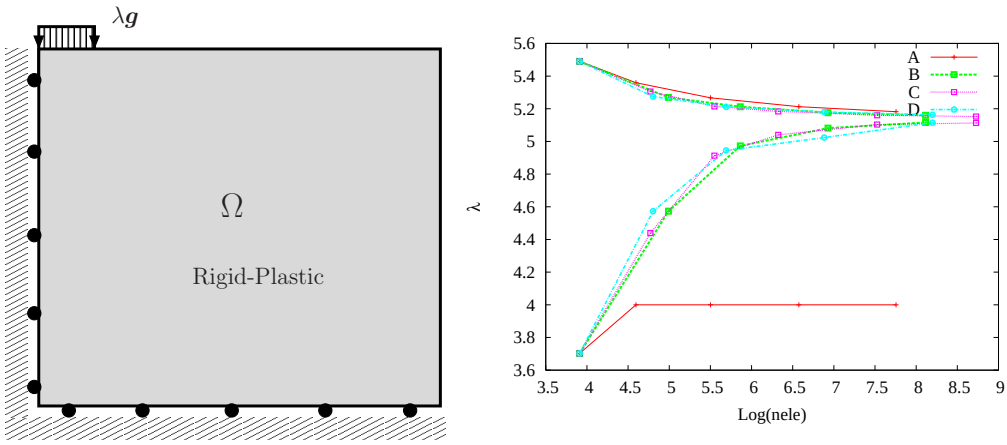

(a) (b)

Figure 2: Strip footing. (a) Geometry and (b) evolution of bounds. The curves correspond to the following 4 cases: adaptive remeshing according to the elemental gap in (19) only (A), additional radial remeshing all around affected nodes with $\eta_u = 0.95$ (B), additional radial remeshing in the directions of the affected elements with $\eta_u = 0.75$ (C), additional radial remeshing all around affected nodes with $\eta_u = 0.25$ (D).

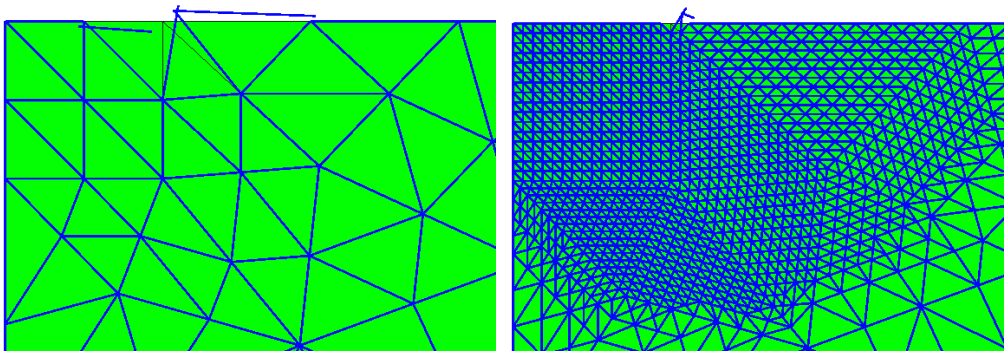

(a) (b)

Figure 3: Strip footing problem. Edge velocities (line elements) and body velocities (equal to zero) with a (a) coarse mesh and (b) a finer mesh.

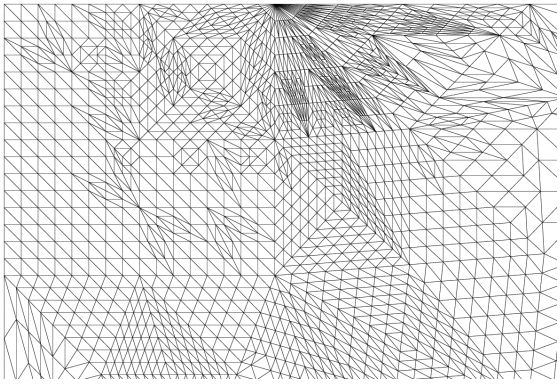

Figure 4: Strip footing problem. Mesh after 4 adaptive remeshing and using radial remeshing.

6.2 Vertical cut

This problem has been analysed in [LS02a, LS02b, LSKH05, KHS05]. The stability of the vertical cut in a purely cohesive soil ($\phi = 0$) is given by the parameter $N_s = H\gamma/c$, where γ is the soil density and c is the cohesion. The tighter computed lower bound for N_s has been reported in [LS02a]. In [LSKH05], an anisotropic error estimate is used, which requires an optimal-mesh adaptive scheme that solves an optimisation problem for the computation of the new element sizes. Our error estimate requires just to evaluate expression (19), and apparently can improve slightly the lower bound given in [LSKH05] for similar number of elements (see values Table 1). A further run with 15214 elements yields the values $N^{LB} = 3.7748$ and $N^{UB} = 3.7849$. As a reference, for the latter mesh and when using a PC with 3GHz and 1GB of RAM, the solution of the SOCP within SDPT3-4.0 took 237 and 438 seconds for the lower and upper bound problem, respectively.

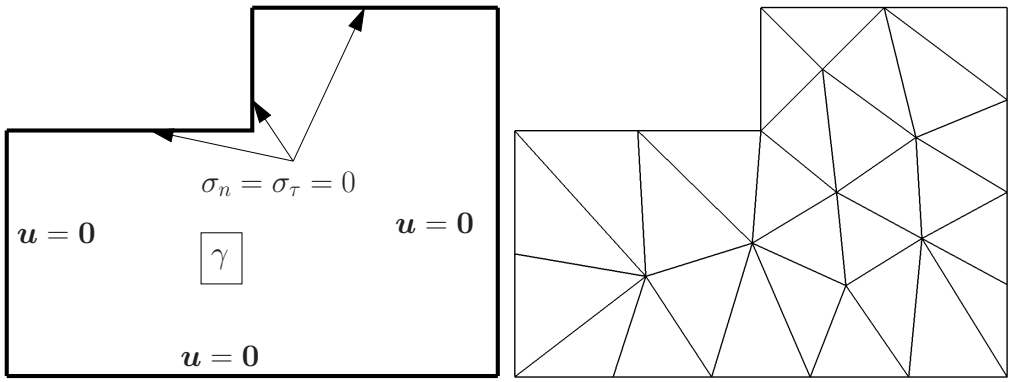

(a) (b)

Figure 5: Vertical cur problem. (a) Geometry and (b) initial mesh.

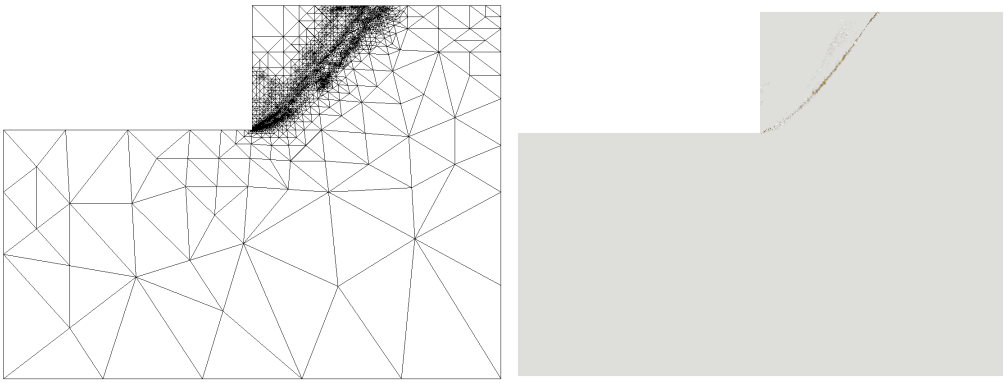

(a) (b)

Figure 6: Vertical cut problem: (a) final mesh employed with 12518 elements and (b) contour plot of Lagrange multipliers for condition $x_1 = 2c$.

6.3 Squared plate with asymmetric holes

This problem has been originally modelled in [DAH00] in the context of viscoplasticity and in compression, and by [ZBS02] using the upper bound theorem. Makrodimopoulos and Martin [MM06] have used the same lower bound interpolation described here, together with the Second Order Conic Programming package MOSEK [ApS05]. However, they have not applied any adaptive remeshing strategy. Thus, we manage to obtain tighter bounds for similar number of elements (see Table 2). In addition, the finer meshes shown in Figure 8 reveal the failure mechanism for a purely cohesive material (Tresca criteria, $c = 1$, $\phi = 0°$), and a cohesive-frictional ($\phi = 30°$) material.

	Lower Bound		Upper Bound	
Reference	# elements	N_s	# elements	N_s
Lyamin et al. [LS02a, LS02b]	2880	3.763	1110	3.801
	6400	3.772	2928	3.794
Lyamin et al. [LSKH05]	500	3.71	-	-
	2000	3.76	-	-
Present work	591	3.7288	591	3.8819
	1994	3.7664	1994	3.8227
	6475	3.7733	6475	3.7964

Table 1: Vertical cut problem. Comparison of bounds obtained by [LS02a], [LSKH05] and in the present work.

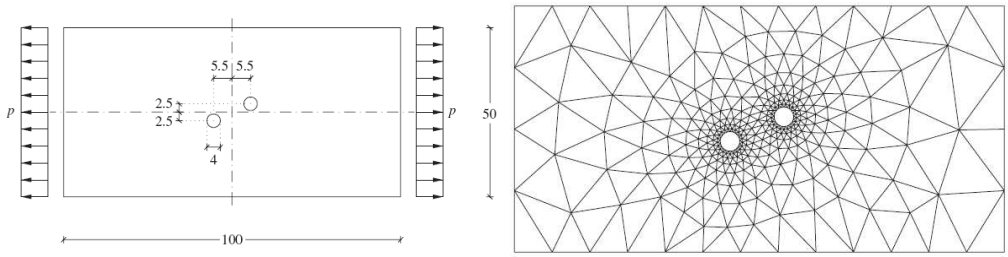

(a) (b)

Figure 7: (a) Geometry and (b) initial mesh employed in the problem of two asymmetric holes.

	$\phi = 0°$		$\phi = 30°$	
Reference	# elements	p/c	# elements	p/c
Makrodimopoulos and Martin [MM06]	2996	1.7840	2996	1.0464
	12738	1.8089	12738	1.0562
Present work	2919	1.8031	1476	1.0542
	10778	1.8112	9227	1.0578

Table 2: Comparison of bounds obtained in [MM06] and in the present work.

7 Conclusions

The main goal and novelty of the article is the design of adaptive remeshing strategy using the solutions of the lower and upper bound limit state problems, while using Second Order Conic Programming (SOCP) for the satisfaction of the plastic criteria. Additionally, the remeshing strategy designed here can deal effectively with problems with discontinuous Neumann conditions.

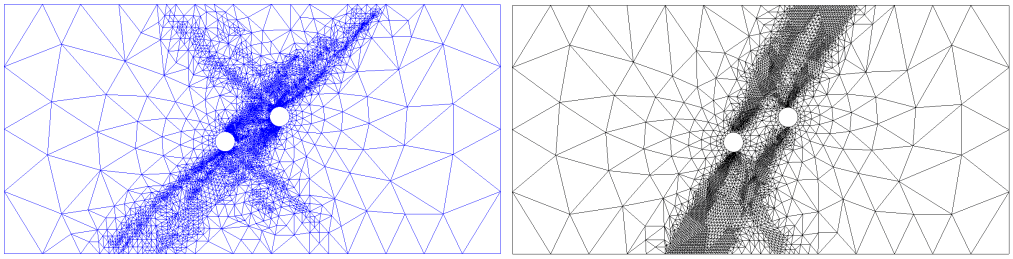

(a) (b)

Figure 8: Final mesh with 10778 elements employed in the problem of 2 asymmetric holes with (a) $\phi = 0^\circ$ and (b) $\phi = 30^\circ$.

A Specific expressions for Von Mises and Mohr-Coulomb plasticity

In Von Mises plasticity, the yield function is given by

$$f(\boldsymbol{\sigma}) = \sqrt{dev\boldsymbol{\sigma} : dev\boldsymbol{\sigma}} - \sqrt{\frac{2}{3}}\sigma_Y, \tag{20}$$

with σ_Y the yield stress. From the associative rule $\boldsymbol{\varepsilon} = \gamma \partial f(\boldsymbol{\sigma})/\boldsymbol{\sigma} = \gamma dev\boldsymbol{\sigma}/\sqrt{dev\boldsymbol{\sigma} : dev\boldsymbol{\sigma}}$, and the definition of the internal work dissipation (7), it follows that $D(\boldsymbol{u})$ and $\varepsilon_{eq}(\boldsymbol{u})$ can be expressed as,

$$\begin{aligned} D(\boldsymbol{u})_{VM} &= \int_\Omega \sigma_Y \varepsilon_{eq,VM} dV \\ \varepsilon_{eq,VM}(\boldsymbol{u}) &= \sqrt{(2/3)\boldsymbol{\varepsilon}(\boldsymbol{u}) : \boldsymbol{\varepsilon}(\boldsymbol{u})}. \end{aligned} \tag{21}$$

In two-dimensional plane strain analysis, the yield function in (20) is expressed as,

$$f(\boldsymbol{\sigma}) = \sqrt{(\sigma_{xx} - \sigma_{yy})^2 + 4\sigma_{xy}^2} - \frac{2}{\sqrt{3}}\sigma_Y.$$

By applying the following transformation of the stress variables $\boldsymbol{\sigma}^{\mathrm{T}} = \{\sigma_{xx}\ \sigma_{yy}\ \sigma_{xy}\}$:

$$\boldsymbol{x}_{24} = \left\{ \begin{array}{c} x_2 \\ x_3 \\ x_4 \end{array} \right\} = \mathbf{M}_{VM}^{-1}\boldsymbol{\sigma}\ ,\ \mathbf{M}_{VM}^{-1} = \left[\begin{array}{ccc} 0 & 0 & 2 \\ 1 & -1 & 0 \\ 1 & 0 & 0 \end{array} \right], \tag{22}$$

the membership constraint $\boldsymbol{\sigma} \in \mathcal{B} = \{\boldsymbol{\sigma} \big| f(\boldsymbol{\sigma}) \leq 0\}$ is equivalent to the following set of constraints:

$$\mathbf{x}_{13} \in \mathcal{L}^3\ ;\ x_1 = \frac{2}{\sqrt{3}}\sigma_Y\ ;\ x_4 \text{ free}, \tag{23}$$

where $\mathcal{L}^3 = \{\mathbf{x} \in \mathbb{R}^3 \big| x_1 \geq \sqrt{x_2^2 + x_3^2}\}$ is the three-dimensional Lorentz cone.

Regarding Mohr-Coulomb plasticity, its yield function is given by,

$$f(\boldsymbol{\sigma}) = \sqrt{2dev\boldsymbol{\sigma} : dev\boldsymbol{\sigma}} + 2\text{trace}(\boldsymbol{\sigma})\sin\phi - 2c\cos\phi \tag{24}$$

with c and ϕ the soil cohesion and internal friction angle. In this case, the following expression for the internal rate of dissipation can be deduced:

$$\begin{aligned} D(\boldsymbol{u})_{MC} &= \int_\Omega 2c\varepsilon_{eq,MC}\cos\phi dV \\ \varepsilon_{eq,MC}(\boldsymbol{u}) &= \sqrt{\boldsymbol{\varepsilon}(\boldsymbol{u}) : \boldsymbol{\varepsilon}(\boldsymbol{u})/(2+2\sin^2\phi)}. \end{aligned} \tag{25}$$

In particular, in two-dimensional plane strain analysis, the yield function in (24) reads

$$f(\boldsymbol{\sigma}) = \sqrt{(\sigma_{xx}-\sigma_{yy})^2 + 4\sigma_{xy}^2} + (\sigma_{xx}+\sigma_{yy})\sin\phi - 2c\cos\phi.$$

By transforming the stress variables as,

$$\mathbf{x}_{13} = \left\{ \begin{array}{c} x_1 \\ x_2 \\ x_3 \end{array} \right\} = \mathbf{M}_{MC}^{-1}\boldsymbol{\sigma} + \mathbf{d}, \tag{26a}$$

with

$$\mathbf{M}_{MC}^{-1} = \left[\begin{array}{ccc} -\sin\phi & -\sin\phi & 0 \\ 0 & 0 & 2 \\ 1 & -1 & 0 \end{array} \right], \ \mathbf{d} = \left\{ \begin{array}{c} 2c\cos\phi \\ 0 \\ 0 \end{array} \right\}, \tag{26b}$$

we can replace the condition $\boldsymbol{\sigma} \in \mathcal{B}$ by $\mathbf{x}_{13} \in \mathcal{L}^3$. If $\phi = 0$, the same transformation used for Von Mises plasticity can be used here, but replacing the equality constraint in (23) $x_1 = \frac{2}{\sqrt{3}}\sigma_Y$ by $x_1 = 2c$.

Note that since matrices $\mathbf{M}_{VM}^{-1}$ and $\mathbf{M}_{MC}^{-1}$ in (22) and (26b) are invertible, we can express $\boldsymbol{\sigma}$ as a function of the $\mathbf{x}$ variables:

$$\boldsymbol{\sigma} = \mathbf{M}_{VM}\mathbf{x}_{24} \ ; \ \boldsymbol{\sigma} = \mathbf{M}_{MC}\mathbf{x}_{13} - \mathbf{M}_{MC}\mathbf{d} \tag{27a}$$

with

$$\mathbf{M}_{VM} = \left[\begin{array}{ccc} 0 & 0 & 1 \\ 0 & -1 & 1 \\ 0.5 & 0 & 0 \end{array} \right], \ \mathbf{M}_{MC} = \frac{1}{2}\left[\begin{array}{ccc} (\sin\phi)^{-1} & 0 & 1 \\ (\sin\phi)^{-1} & 0 & -1 \\ 0 & 1 & 0 \end{array} \right]. \tag{27b}$$

B Discrete lower bound problem

We write next the algebraic form of the discrete lower bound problem in (13). Full details of the implementation can be found in [Cir04, Gut05], and we will give here the mean steps towards the construction of the final optimisation problem.

For each element e, we denote the elemental stress vector by $\boldsymbol{\sigma}^{e\mathrm{T}} = \{\boldsymbol{\sigma}^{e,1\mathrm{T}}\ \boldsymbol{\sigma}^{e,2\mathrm{T}}\ \boldsymbol{\sigma}^{e,3\mathrm{T}}\}$, with $\boldsymbol{\sigma}^{e,n\mathrm{T}} = \{\sigma^{e,n}_{xx}\ \sigma^{e,n}_{yy}\ \sigma^{e,n}_{xy}\},\ n = 1,2,3$ the nodal stresses. On the other hand, we note that since the stresses are linear, imposing the second and third equality constraints at the whole edge is equivalent to impose them at each node of the edge. Consequently, the first two equality constraints in (13) may be then written as,

$$\mathbf{A}^e\boldsymbol{\sigma}^e + \lambda\mathbf{f}^e = \mathbf{0}; e = 1,\dots,nele \tag{28a}$$

$$\mathbf{N}^n\boldsymbol{\sigma}^{n,e} + \lambda\mathbf{g}^{n,e} = \mathbf{0}; e,n \in \xi^g \tag{28b}$$

where ξ^g is the set of external boundaries with Neumann conditions, and condition (28a) is imposed at the nodes connected to those edges, with normal vector $\boldsymbol{n}^{\mathrm{T}}_{\xi^g} = \{n_x\ n_y\}$. The matrices A^e and $\mathbf{N}^e$ are given by,

$$\mathbf{A}^e = \left[\mathbf{D}^1\ \mathbf{D}^2\ \mathbf{D}^3\right]\ ;\ \mathbf{D}^n = \begin{bmatrix} I^n_{,x} & 0 & I^n_{,y} \\ 0 & I^n_{,y} & I^n_{,x} \end{bmatrix} \tag{29a}$$

$$\mathbf{N}^n = \begin{bmatrix} n_x & 0 & n_y \\ 0 & n_y & n_x \end{bmatrix} \tag{29b}$$

where $I^n_{,x}$ and $I^n_{,y}$ are the derivatives of the interpolating functions of node n with respect to x and y, respectively. Note that, in order to ensure exact equilibrium, we have to assume that the body loads $\boldsymbol{f}$ and the surface loads $\boldsymbol{g}$ are, at most, constant at each element and linear at each edge, respectively. Their elemental and nodal values are given in the vectors $\mathbf{f}^e$ and $\mathbf{g}^{n,e}$ in (28). The third equality constraint in (13) is the equilibrium equation at the internal edges. Any pair of elements e and e', with a common edge $\xi^e_{e'}$ and with normal vector $\boldsymbol{n}^e_{e'}$, leads to two nodal equations that are expressed as,

$$\mathbf{N}^n\boldsymbol{\sigma}^{n,e} - \mathbf{N}^n\boldsymbol{\sigma}^{n,e'} = \mathbf{0}; e,e',n \in \xi^e_{e'}, \tag{30}$$

where $\mathbf{N}^n$ has the same form as in (29b). The assembling of the elemental (28) and (30), together with the membership constraint in (13) leads to the following global optimisation problem:

$$\begin{array}{l} \max \lambda \\ s.t. \left\{ \begin{array}{l} \begin{bmatrix} \mathbf{f} & \mathbf{A} \\ \mathbf{g} & \mathbf{N}^g \\ \mathbf{0} & \mathbf{N}^e_{e'} \end{bmatrix} \left\{ \begin{array}{c} \lambda \\ \boldsymbol{\sigma}^{LB} \end{array} \right\} = \mathbf{0} \\ \boldsymbol{\sigma}^{e,n} \in \mathcal{B},\ n = 1,2,3; e = 1,\dots,nele. \end{array} \right. \end{array} \tag{31}$$

Matrix $\mathbf{A}$ and vectors $\mathbf{f}$and $\mathbf{g}$ are the assembling of the elemental and nodal contributions of $\mathbf{A}^e$, $\mathbf{f}^e$ and $\mathbf{g}^e$, respectively, whereas matrices $\mathbf{N}^g$ and $\mathbf{N}^e_{e'}$ are the assembled nodal matrices $\mathbf{N}^n$ in (28b) and (30), respectively. The vector $\boldsymbol{\sigma}^{LB}$ corresponds to the whole set of nodal stresses, and has $3 \times 3 \times nele$ scalar components. In order to write the membership constraint as a second order conic constraint, a linear transformation of the nodal stresses is required. It is shown in Appendix A that in Von Mises plasticity or in Mohr-Coulomb with $\phi = 0$, it is convenient to introduce the variable $\mathbf{x}^{n,e}_{14} = \{x^{n,e}_1\ x^{n,e}_2\ x^{n,e}_3\ x^{n,e}_4\}$ and use the elemental transformation:

$$\boldsymbol{\sigma}^{n,e} = \mathbf{M}_{VM}\mathbf{x}^{n,e}_{24}, \tag{32}$$

together with the condition $x_1 = 2\sigma_Y/\sqrt{3}$ or $x_1 = 2c$. In Mohr-Coulomb plasticity with $\phi \neq 0$, we use the variable $\mathbf{x}^{n,e}_{13} = \{x^{n,e}_1\ x^{n,e}_2\ x^{n,e}_3\}$ and the transformation:

$$\boldsymbol{\sigma}^{n,e} = \mathbf{M}_{MC}\mathbf{x}^{n,e}_{13} - \mathbf{M}_{MC}\mathbf{d} \tag{33}$$

Explicit expressions for the matrices $\mathbf{M}_{VM}$, $\mathbf{M}_{MC}$ and vector $\mathbf{d}$ are given in equations (26b) and (27) of Appendix A. Inserting the transformation (32) into the constraints in (31) yields the following optimisation problem:

$$\begin{array}{l} \max \lambda \\ s.t. \left\{ \begin{array}{l} \left[\begin{array}{ccc} \mathbf{f} & \mathbf{0} & \mathbf{A}_M \\ \mathbf{g} & \mathbf{0} & \mathbf{N}^g_M \\ \mathbf{0} & \mathbf{0} & \mathbf{N}^e_{e'M} \\ \mathbf{0} & \mathbf{I} & \mathbf{0} \end{array}\right] \left\{ \begin{array}{c} \lambda \\ \mathbf{x}^{LB}_1 \\ \mathbf{x}^{LB}_{24} \end{array} \right\} = \left\{ \begin{array}{c} \mathbf{0} \\ \mathbf{0} \\ \mathbf{0} \\ \boldsymbol{b} \end{array} \right\} \\ \mathbf{x}^{LB}_4, \lambda \text{ free}, \mathbf{x}^{LB}_{13} \in \underbrace{\mathcal{L}^3 \times \ldots \times \mathcal{L}^3}_{3\times 3\times nele} \end{array} \right. , \end{array} \tag{34}$$

valid in Von Mises or Mohr-Coulomb plasticity with $\phi = 0$. For each plastic model, the vector $\mathbf{b}$ is given by $\mathbf{b}^{\mathrm{T}}_{VM} = 2\sigma_Y/\sqrt{3}\{1\ \ldots\ 1\}_{3\times nele}$ and $\mathbf{b}^{\mathrm{T}}_{MC} = 2c\{1\ \ldots\ 1\}_{3\times nele}$, respectively. The matrices $\mathbf{A}_M$, $\mathbf{N}^g_M$ and $\mathbf{N}^e_{e'M}$ are the assembling of the elemental products $\mathbf{A}^e\mathbf{M}$ and nodal products $\mathbf{N}^n\mathbf{M}$. The global vectors $\mathbf{x}^{LB}_1$ and $\mathbf{x}^{LB}_{24}$ have the following components $\mathbf{x}^{LB^{\mathrm{T}}}_1 = \{x^{1,1^{\mathrm{T}}}_1 \ldots \mathbf{x}^{3,nele^{\mathrm{T}}}_1\}_{3\times nele}$ and $\mathbf{x}^{LB^{\mathrm{T}}}_{24} = \{\mathbf{x}^{1,1}_{24} \ldots \mathbf{x}^{3,nele}_{24}\}_{3\times 3\times nele}$.

A slightly shorter expression than (34) is obtained when inserting transformation (33) into (31), which gives rise to the lower bound optimisation problem in Mohr-Coulomb plasticity with $\phi \neq 0$:

$$\max \lambda$$
$$s.t. \left\{ \begin{array}{l} \left[\begin{array}{cc} \mathbf{f} & \mathbf{A}_M \\ \mathbf{g} & \mathbf{N}_M^g \\ \mathbf{0} & \mathbf{N}_{e'M}^e \end{array} \right] \left\{ \begin{array}{c} \lambda \\ \mathbf{x}_{13}^{LB} \end{array} \right\} = \left\{ \begin{array}{c} -\mathbf{d}_{AM} \\ -\mathbf{d}_{NM} \\ \mathbf{0} \end{array} \right\} \\ \lambda \text{ free}, \mathbf{x}_{13}^{LB} \in \underbrace{\mathcal{L}^3 \times \ldots \times \mathcal{L}^3}_{3\times 3\times nele} \end{array} \right. , \tag{35}$$

where $\mathbf{d}_{AM}$ and $\mathbf{d}_{NM}$ are the assembling of the elemental products $\mathbf{A}^e\mathbf{M}_{MC}\mathbf{d}$ and $\mathbf{N}^n\mathbf{M}_{MC}\mathbf{d}$. The three-dimensional Lorentz cone $\mathcal{L}^3$ is defined by $\mathcal{L}^3 = \{\mathbf{x} \in \mathbb{R}^3 \big| x_1 \geq \sqrt{x_2^2 + x_3^2}\}$.

C Discrete upper bound problem

Inserting the membership constraints for the edge tensions $\boldsymbol{t}^{UB}$, the optimisation problem in (15) turns into,

$$\sup \lambda$$
$$s.t. \left\{ \begin{array}{l} a(\boldsymbol{\sigma}^{UB}, \boldsymbol{v}^{UB}) = \lambda \ell(\boldsymbol{v}^{UB}),\ \forall \boldsymbol{v}^{UB} \in \mathcal{U}^{UB} \\ \boldsymbol{t}^{UB} \in \mathcal{B}_t^{UB} \\ \boldsymbol{\sigma}^{UB} \in \mathcal{B}^{UB}. \end{array} \right. \tag{36}$$

where $\boldsymbol{\sigma}^{UB} = \{\boldsymbol{\sigma}^{1^{\mathrm{T}}} \ldots \boldsymbol{\sigma}^{nele^{\mathrm{T}}}\}_{3\times nele}$ and $\mathbf{v}^{UB} = \{\mathbf{v}^{1^{\mathrm{T}}} \ldots \mathbf{v}^{nele^{\mathrm{T}}}\}_{2\times 3\times nele}$ are the global vectors of stresses and velocities. Their elemental components are given by $\boldsymbol{\sigma}^e = \{\sigma_{xx}^e\ \sigma_{yy}^e\ \sigma_{xy}^e\}$ and $\mathbf{v}^{e^{\mathrm{T}}} = \{\mathbf{v}^{1,e^{\mathrm{T}}}\ \mathbf{v}^{2,e^{\mathrm{T}}}\ \mathbf{v}^{3,e^{\mathrm{T}}}\}$. In addition, we denote by $\mathbf{t}^{e-e^{\mathrm{T}}} = \{\mathbf{t}^{1,e-e'^{\mathrm{T}}}\ \mathbf{t}^{2,e-e'^{\mathrm{T}}}\}$ the nodal tensions at the edge $\xi_{e'}^e$. In order to recast (36) in a standard optimisation form, we first note that, recalling the nodal matrices $\mathbf{D}^n$ in (29a), the elemental contribution of the terms in $a(,)$ and $\ell()$ may be written as,

$$\begin{aligned} \sum_{e=1,nele} a(\boldsymbol{\sigma}^e, \boldsymbol{v}^e) &= \sum_{e=1,nele} \mathbf{v}^e \cdot \int_{\Omega^e} \left[\begin{array}{c} \mathbf{D}^1 \\ \mathbf{D}^2 \\ \mathbf{D}^3 \end{array} \right] dV \boldsymbol{\sigma}^e + \sum_{e,e'\in\xi_{e'}^e} \int_{\xi_{e'}^e} \boldsymbol{t}^{e-e'}(\boldsymbol{v}^e - \boldsymbol{v}^{e'}) d\Gamma \\ &= \sum_{e=1,nele} \mathbf{v}^e \cdot \tilde{\mathbf{A}}\boldsymbol{\sigma}^e + \sum_{e,e'\in\xi_{e'}^e} \mathbf{v}^{e-e'} \cdot \mathbf{B}^e \mathbf{t}^{e-e'} \\ &= \mathbf{v}^{UB} \cdot \left(\mathbf{A}\boldsymbol{\sigma}^{UB} + \mathbf{B}\mathbf{t}^{UB}\right) \end{aligned} \tag{37}$$

$$\sum_{e=1,nele} \int_{\Omega^e} \boldsymbol{v}^e \cdot \boldsymbol{f} dV = \sum_{e=1,nele} \sum_{n=1,2,3} \mathbf{v}^{n,e} \cdot \int_{\Omega^e} I^n \boldsymbol{f} dV = \sum_{e=1,nele} \mathbf{v}^e \cdot \mathbf{f}^e = \mathbf{v}^{UB} \cdot \mathbf{f}$$

$$\sum_{e\in\Gamma_g} \int_{\Gamma_g^e} \boldsymbol{v}^e \cdot \boldsymbol{g} dV = \sum_{e\in\Gamma_g} \sum_{n\in\Gamma_g^e} \mathbf{v}^{n,e} \cdot \int_{\Gamma_g^e} I^n \boldsymbol{g} dV = \sum_{e\in\Gamma_g} \mathbf{v}^e \cdot \mathbf{g}^e = \mathbf{v}^{UB}\mathbf{g}$$

where $\tilde{\mathbf{A}}^{e\mathrm{T}} = \int_{\Omega^e} \left[\mathbf{D}^{1\mathrm{T}}\ \mathbf{D}^{2\mathrm{T}}\ \mathbf{D}^{3\mathrm{T}}\right] dV$. The nodal velocities at the edges $\mathbf{v}_\xi^{e-e'}$ and the elemental matrix $\mathbf{B}^e$ are given by

$$\mathbf{v}_\xi^{e-e'} = \left\{ \begin{array}{c} \mathbf{v}^{1,e} \\ \mathbf{v}^{2,e} \\ \mathbf{v}^{1,e'} \\ \mathbf{v}^{2,e'} \end{array} \right\}\ ,\ \mathbf{B}^e = \left[\begin{array}{cc} \tilde{\mathbf{I}}^{11} & \tilde{\mathbf{I}}^{12} \\ \tilde{\mathbf{I}}^{21} & \tilde{\mathbf{I}}^{22} \\ -\tilde{\mathbf{I}}^{11} & -\tilde{\mathbf{I}}^{12} \\ -\tilde{\mathbf{I}}^{21} & -\tilde{\mathbf{I}}^{22} \end{array} \right]\ ,\ \tilde{\mathbf{I}}^{ij} = I_\xi^i I_\xi^j \mathbf{I}_2$$

with $\mathbf{I}_2$ the 2×2 unit matrix and $I_\xi^n, n = 1, 2$ the nodal interpolating functions at the edges. The elemental vectors $\mathbf{f}^e$ and $\mathbf{g}^e$ in (37) are two elemental vectors associated to the body and surface loads. Matrices $\tilde{\mathbf{A}}$ and $\mathbf{B}$, and vectors $\mathbf{f}$ and $\mathbf{g}$ are the assembled elemental contributions of $\tilde{\mathbf{A}}^e$, $\mathbf{B}^e$, $\mathbf{f}^e$ and $\mathbf{g}^e$, respectively.

With this notation at hand, the condition $a(\boldsymbol{\sigma}^{UB}, \boldsymbol{v}^{UB}) = \lambda \ell(\boldsymbol{v}^{UB}), \forall \boldsymbol{v}^{UB} \in \mathcal{U}^{UB}$ is equivalent to the following system of equations:

$$\tilde{\mathbf{A}}\boldsymbol{\sigma}^{UB} + \mathbf{B}\mathbf{t}^{UB} - \lambda(\mathbf{f} + \mathbf{g}) = \mathbf{0}. \tag{38}$$

Regarding the tension membership constraints, for each interior each $\xi_{e'}^e$, the Von Mises condition (17) is applied to the two nodal tensions $\mathbf{t}^{1,e-e'}$ and $\mathbf{t}^{2,e-e'}$ as follows:

$$\begin{array}{l} t_T^{n,e-e'} - s_{2n-1} = \sigma_Y/\sqrt{3}\ ;\ s_1 \geq 0 \quad ,\ n = 1, 2 \\ -t_T^{n,e-e'} - s_{2n} = \sigma_Y/\sqrt{3}\ ;\ s_2 \geq 0 \quad ,\ n = 1, 2, \end{array} \tag{39a}$$

whereas the Mohr-Coulomb condition (18) may be written in a similar manner,

$$\begin{array}{l} t_T^{n,e-e'} - s_{2n-1} = c + t_N^{n,e-e'} \tan\phi\ ;\ s_1 \geq 0 \quad ,\ n = 1, 2 \\ -t_T^{n,e-e'} - s_{2n} = c + t_N^{n,e-e'} \tan\phi\ ;\ s_2 \geq 0 \quad ,\ n = 1, 2. \end{array} \tag{39b}$$

Both conditions in (39) can be expressed in the following compact form:

$$\mathbf{T}^e \mathbf{t}^{e-e'} + \mathbf{I}_4 \mathbf{s}^e = \mathbf{b}_t^e, \tag{40a}$$

where $\mathbf{s}^{e\mathrm{T}} = \{s_1\ s_2\ s_3\ s_4\}$, $\mathbf{I}_4$ is the 4×4 unit matrix, and the matrix $\mathbf{T}^e$ and vector $\mathbf{b}_t^e$ have the following expressions for each plastic model:

$$\mathbf{T}^e_{VM} = \begin{bmatrix} 0 & 1 & 0 & 0 \\ 0 & -1 & 0 & 0 \\ 0 & 0 & 0 & 1 \\ 0 & 0 & 0 & -1 \end{bmatrix} \begin{bmatrix} \mathbf{R} & \mathbf{0} \\ \mathbf{0} & \mathbf{R} \end{bmatrix} \quad , \; \mathbf{b}^e_{tVM} = \frac{\sigma_Y}{\sqrt{3}} \begin{Bmatrix} 1 \\ 1 \\ 1 \\ 1 \end{Bmatrix},$$

$$\mathbf{T}^e_{MC} = \begin{bmatrix} -\tan\phi & 1 & 0 & 0 \\ -\tan\phi & -1 & 0 & 0 \\ 0 & 0 & -\tan\phi & 1 \\ 0 & 0 & -\tan\phi & -1 \end{bmatrix} \begin{bmatrix} \mathbf{R} & \mathbf{0} \\ \mathbf{0} & \mathbf{R} \end{bmatrix} \quad , \; \mathbf{b}^e_{tMC} = c \begin{Bmatrix} 1 \\ 1 \\ 1 \\ 1 \end{Bmatrix}. \tag{40b}$$

Matrix $\mathbf{R}$ is a two-dimensional rotation matrix that transforms the nodal tensions vectors $\mathbf{t}^{i,e}, i = 1, 2$ in $x - y$ components into the local components aligned with the edge $\xi^e_{e'}$.

Gathering the constraints (38) and (40), we can rewrite the upper bound optimisation problem in (36) as,

$$\begin{aligned} &\max \lambda \\ &s.t. \begin{cases} \begin{bmatrix} -\mathbf{f} - \mathbf{g} & \mathbf{B} & \mathbf{0} & \tilde{\mathbf{A}} \\ \mathbf{0} & \mathbf{T} & \mathbf{I} & \mathbf{0} \end{bmatrix} \begin{Bmatrix} \lambda \\ \mathbf{t}^{UB} \\ \mathbf{s} \\ \boldsymbol{\sigma}^{UB} \end{Bmatrix} = \begin{Bmatrix} \mathbf{0} \\ \mathbf{b}_t \end{Bmatrix} \quad , \\ \lambda, \mathbf{t}^{UB} \text{free}, \mathbf{s} \geq 0, \boldsymbol{\sigma}^{UB} \in \mathcal{B}^{UB}. \end{cases} \end{aligned} \tag{41}$$

with $\mathbf{T}$,$\mathbf{b}_t$ and $\mathbf{s}$ the assembled elemental contributions $\mathbf{T}^e$, $\mathbf{b}^e_t$ and $\mathbf{s}^e$ in (40).

In order to write the stress membership constraint as a SOCP, we resort to the same technique employed in the lower bound method. In the present case, though, the stresses field is elemental, not nodal, and thus, we will use the transformations in (27) but applied to the elemental stresses $\boldsymbol{\sigma}^e$. The resulting optimisation problem in Von Mises plasticity or Mohr-Coulomb with $\phi = 0$ reads,

$$\begin{aligned} &\sup \lambda \\ &s.t. \begin{cases} \begin{bmatrix} -\mathbf{f} - \mathbf{g} & \mathbf{B} & \mathbf{0} & \mathbf{0} & \tilde{\mathbf{A}}_M \\ \mathbf{0} & \mathbf{T} & \mathbf{0} & \mathbf{I} & \mathbf{0} \\ \mathbf{0} & \mathbf{0} & \mathbf{I} & \mathbf{0} & \mathbf{0} \end{bmatrix} \begin{Bmatrix} \lambda \\ \mathbf{t}^{UB} \\ \mathbf{x}^{UB}_1 \\ \mathbf{s} \\ \mathbf{x}^{UB}_{24} \end{Bmatrix} = \begin{Bmatrix} \mathbf{0} \\ \mathbf{b}_t \\ \mathbf{b} \end{Bmatrix} \quad , \\ \lambda, \mathbf{t}^{UB}, \mathbf{x}^{UB}_4 \text{free}, \mathbf{s} \geq 0, \mathbf{x}^{UB}_{13} \in \underbrace{\mathcal{L}^3 \times \ldots \times \mathcal{L}^3}_{3 \times nele}. \end{cases} \end{aligned} \tag{42a}$$

where the vector $\mathbf{b}$ is given by $\mathbf{b}_{VM}^{\mathrm{T}} = 2\sigma_Y/\sqrt{3}\{1\ \ldots\ 1\}_{nele}$ and $\mathbf{b}_{MC}^{\mathrm{T}} = 2c\{1\ \ldots\ 1\}_{nele}$ in Von Mises and Mohr Coulomb plasticity, respectively. For Mohr-Coulomb with $\phi \neq 0$ we obtain,

$$\begin{array}{l} \sup \lambda \\ s.t. \left\{ \begin{array}{l} \left[\begin{array}{cccc} -\mathbf{f}-\mathbf{g} & \mathbf{B} & \mathbf{0} & \tilde{\mathbf{A}}_M \\ \mathbf{0} & \mathbf{T} & \mathbf{I} & \mathbf{0} \end{array} \right] \left\{ \begin{array}{c} \lambda \\ \mathbf{t}^{UB} \\ \mathbf{s} \\ \mathbf{x}_{13}^{UB} \end{array} \right\} = \left\{ \begin{array}{c} -\mathbf{d}_{AM} \\ \mathbf{b}_t \end{array} \right\} \\ \lambda, \mathbf{t}^{UB}\text{free}, \mathbf{s} \geq 0, \mathbf{x}_{13}^{UB} \in \underbrace{\mathcal{L}^3 \times \ldots \times \mathcal{L}^3}_{3\times nele}. \end{array} \right. \end{array} \quad . \tag{42b}$$

The matrix $\tilde{\mathbf{A}}_M$ and vector $\mathbf{d}_{AM}$ are the assembling of the elemental contributions $\tilde{\mathbf{A}}^e\mathbf{M}$ and $\mathbf{Md}$, with $\mathbf{M}$ and $\mathbf{d}$ in (27b) and (26b).

D Analysis of the lower bound problem with singular surface loads

The need for fan-type mesh distribution around points with discontinuous Neumann conditions was already pointed out by [Che75] when analysing the strip footing problem with the lower bound theorem and adding discontinuities in the stress field. This discontinuities allow variations in the direction of the principal stress along elements with constant stresses. This fact was recognised in [Che75] when subdividing the rigid-plastic domain in sub-domains that are in static equilibrium.

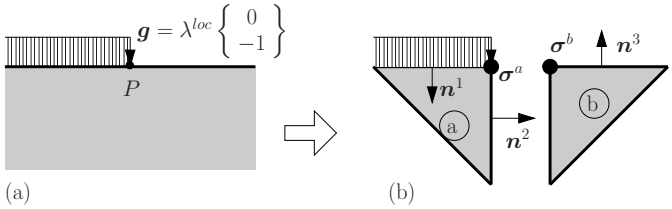

Figure 9: (a) Continuum problem and (b) simplified model with 2 elements used for the analysis of the lower bound problem.

In the context of the discretised stress and velocity fields used here (which are also employed in [LS02a, MM06]), we first analyse the simple problem depicted in Figure 9. The vertical surface load $\boldsymbol{g}^{\mathrm{T}} = \{0,\ -1\}$ is applied along a free surface, with a discontinuity at point P. The domain around P is discretised with 2 elements, a and b, which are connected at point P at the nodes also denoted a and b (see Figure 9b). The maximum load factor for the local system considered here, in case it exist, is denoted λ^{loc}. According to the lower bound problem described in Section 3, the stress is piecewise linear, and thus discontinuity is allowed at the top Neumann boundaries and at the vertical internal edge given by the normals $\boldsymbol{n}^1$, $\boldsymbol{n}^3$ and $\boldsymbol{n}^2$. However, in order to guarantee

a rigorous lower bound, equilibrium is enforced at these boundaries, or equivalently, at nodes a and b due to the linearity of the stress field. Consequently, the following nodal equilibrium equations are obtained:

$$\begin{aligned} \boldsymbol{\sigma} \cdot \boldsymbol{n}^1 &= \lambda^{loc} \boldsymbol{g}, \\ (\boldsymbol{\sigma}^a - \boldsymbol{\sigma}^b) \cdot \boldsymbol{n}^2 &= \mathbf{0}, \\ \boldsymbol{\sigma}^b \cdot \boldsymbol{n}^3 &= \mathbf{0}. \end{aligned}$$

It can be verified that the previous equations allow to write the stresses at a and b as

$$\begin{aligned} \boldsymbol{\sigma}^{a\mathrm{T}} &= \{\sigma,\ 0,\ -\lambda^{loc}\} \\ \boldsymbol{\sigma}^{b^{\mathrm{T}}} &= \{\sigma,\ 0,\ 0\}, \end{aligned} \tag{43}$$

where σ is a free variable. In addition, the admissibility of the stresses $\boldsymbol{\sigma}^a$ and $\boldsymbol{\sigma}^b$, for the Von Mises yield surface with yield stress σ_y, gives rise, after taking into account equations (43), to the following conditions:

$$\begin{aligned} \boldsymbol{\sigma}^2 + (\lambda^{loc})^2 + \sigma\lambda^{loc} &\leq \sigma_y^2 \\ \sigma^2 &= \sigma_y^2. \end{aligned} \tag{44}$$

The maximum value of λ that satisfies these conditions is given by $\lambda^{loc} = 2\sigma_y/\sqrt{3}$, which is obtained for $\sigma = -\sigma_y/\sqrt{3}$. Three main conclusions can be drawn from this result:

1 A maximum value for λ^{loc} has been found. The lower bound problem searches the maximum value of $\lambda = \lambda^{LB}$ that satisfies all the discretised equilibrium equations in the whole domain. Therefore, in a mesh that contains the local simplified system given above, the values found provide a limitation in the maximum value, i.e. $\lambda^{UB} \leq \lambda^{loc}$.

2 Any remeshing strategy of the two elements considered with the pattern in Figure 1a leads to a identical problem as the one considered here, and thus leaves the value of λ^{loc} unchanged.

3 If we add one additional element around point P, let's say element c, we are adding three more variables $\boldsymbol{\sigma}^c$, and two more equilibrium equations at the internal edge, plus one more yield condition for $\boldsymbol{\sigma}^c$. Therefore, if the new conditions are independent of the previous ones, the limitation found for the local problem always exists, independently of the number of elements.

In order to verify numerically the last remark, we have modelled the simplified model for different opening angles α of the two free surfaces and for different number of elements $nele$ (see Figure 10). In addition, for the case $\alpha = 180°$, we have only added elements within a central angle β. The evolution of the λ^{loc} is plotted in Figure 11. Two further conclusions can be extracted:

4 In agreement with point 3 above, a maximum value λ^{loc} is always found.

5 It has been verified in Figure 11 that for values of $\beta > 90°$, the load factor λ^{loc} converges to the exact solution $(2+\pi)c = 5.141592$. Although it can not be appreciated in the Figure, for $\beta = 80$, the limit $\lambda^{loc} = 5.31805$ is obtained (tests until $nele = 1000$ have been performed).

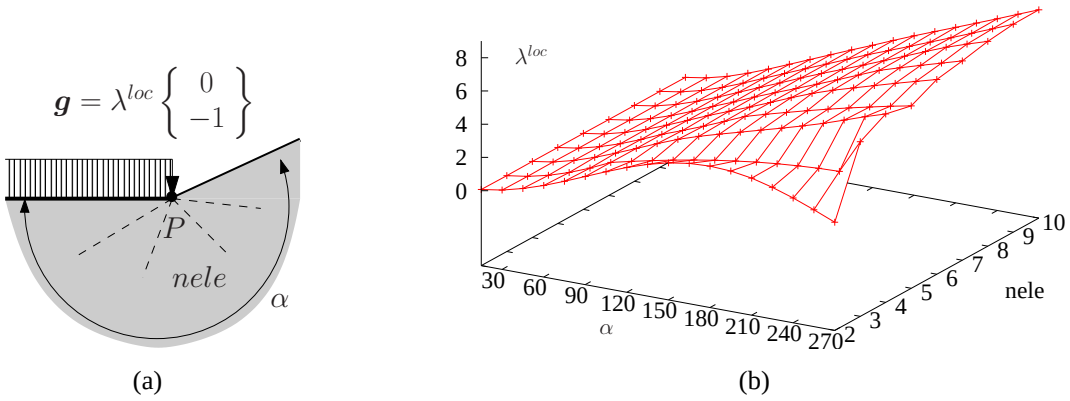

Figure 10: Values of λ^{loc} as a function of α and $nele$.

We found the last point relevant in two senses. First, there is no need to remesh radially in all directions, and thus it appears reasonable to design a strategy that concentrates elements in those directions that constrain the maximisation problem. Second, the load factor of the rigid strip footing has been found by only searching the solution of a local constrained problem. This means that if the velocity and stress field at the limit load are not desired, a strict lower bound of the load factor may be computed by just analysing the reduced model, which is computational much cheaper than modelling the whole domain. Furthermore, from the tightness of the λ^{loc}, we can deduce that the load factor of the non-discretised studied problem is determined by a local phenomenon, independently of the fracture lines (or velocity and stress field).

We have performed the same analysis for a Mohr-Coulomb material, and the same conclusions have been found. Instead of the value $N_s = (2+\pi)c$ though, the solution converged towards the Prandt solution given by [Che75, Pra20]:

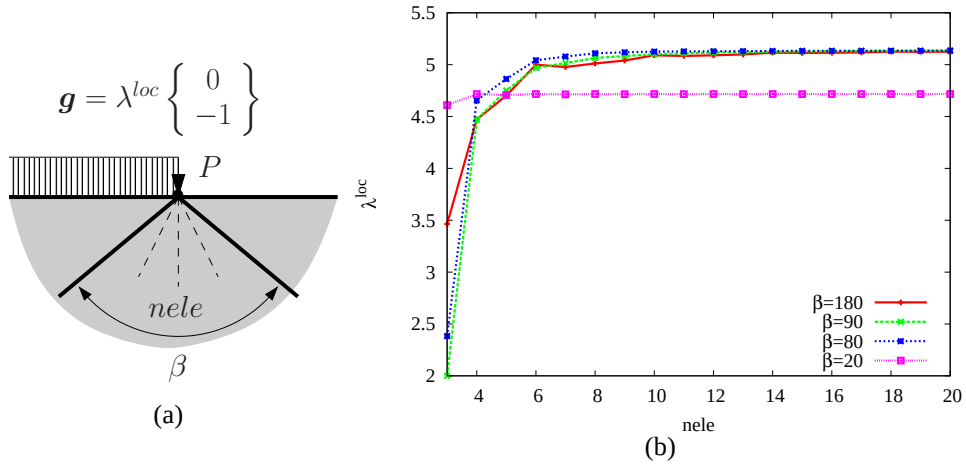

Figure 11: Values of λ^{loc} for $\alpha = 180^\circ$ and different number of elements within different centred angles β.

$$\lambda = c\left(e^{\pi \tan\phi} \tan^2(45 + \phi/2) - 1\right) \cot\phi$$

In particular, for the values $c = 1$ and $\phi = 30^\circ$, this expression yields $\lambda = 30.13962$, which is the limit value of the local problem (see Figure 12). Whether the observed behaviour for the strip footing can be extended in 3D for a footing slab must still be investigated.

REFERENCES

[ApS05] MOSEK ApS. The MOSEK optimization tools version 3.2 (Revision 8). *User's Manual and Reference*, 2005. Avail. http://www.mosek.com.

[BV04] S Boyd and L Vandenberghe. *Convex Optimization*. Cambridge Univ. Press, 2004.

[BZCF01] L Borges, N Zouain, C Costa, and R Feijóo. An adaptive approach to limit analysis. *Int. J. Solids Struct.*, 38:1707–1720, 2001.

[CA99] E Christiansen and K D Andersen. Computation of collapse states with von mises type yield condition. *Int. J. Num. Meth. Engng.*, 46:1185–1202, 1999.

[Che75] W F Chen. *Limit analysis and soil plasticity*. Dev. in Geoth. Engin. 7. Elsevier, 1975.

[Chr96] E Christiansen. *Handbook of Numerical Analysis, vol IV*, volume IV, chapter II, Limit Analysis of Collapse States, pages 193–312. North Holland Amsterdam, 1996.

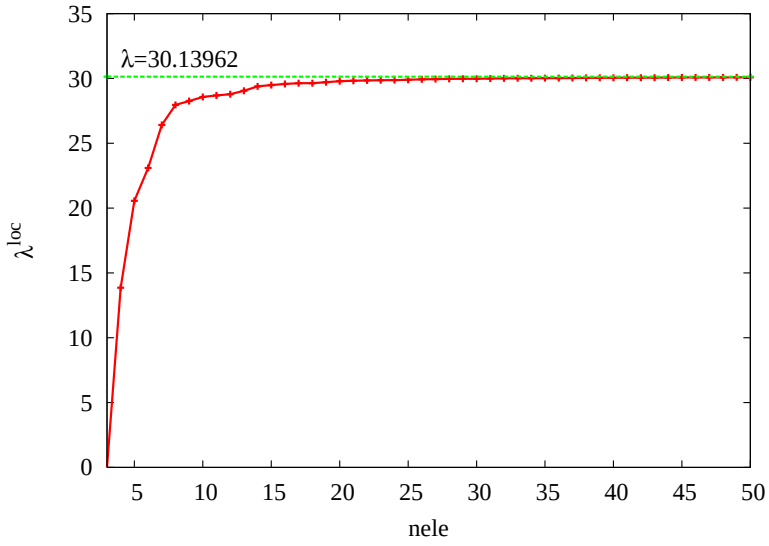

Figure 12: Evolution of λ^{loc} as a function of the number of elements for a Mohr-Coulomb material with $c = 1$ and $\phi = 30°$.

[Cir04] H Ciria. *Computation of Upper and Lower Bounds in Limit State Analysis using Second-Order Cone Programming and Mesh Adaptivity*. PhD thesis, Dep. Aeron. and Astron, MIT, USA, 2004.

[CP01] E Christiansen and O S Pedersen. Automatic mesh refinement in limit analysis. *Int. J. Num. Meth. Engng.*, 50:1331–1346, 2001.

[DÓ5] J M Díaz. *Análisis en estado límite para suelos: cálculo de cotas exactas empleando el modelo Mohr-Coulomb mediante programación cónica de segundo orden.* PhD thesis, ETSCCP, 2005.

[DAH00] P Díez, M Arroyo, and A Huerta. Adaptivity based on error estimation for viscoplastic softening materials. *Mech. Cohesive-Fric. Mat.*, 5:87=112, 2000.

[Gut05] R Gutiérrez. *Evaluación de cotas estrictas para el análisis en estado límite de geomateriales mediante programación cónica de segundo orden.* PhD thesis, ETSCCP, 2005.

[KD03] K Krabbenhoft and L Damkilde. A general non-linear optimization algorithm for lower bound limit analysis. *Int. J. Num. Meth. Engng.*, 56:165–184, 2003.

[KHS05] K Krabbenhoft, A V Lyamin M Hjiaj, and S W Sloan. A new discontinuous upper bound limit analysis formulation. *Int. J. Num. Meth. Engng.*, 63:1069–1088, 2005.

[LS02a] A V Lyamin and S W Sloan. Lower bound limit analysis using non-linear programming. *Int. J. Num. Meth. Engng.*, 55:576–611, 2002.

[LS02b] A V Lyamin and S W Sloan. Upper bound limit analysis using linear finite elements and non-linear programming. *Int. J. Num. Anal. Meth. Geomech.*, 26:181–216, 2002.

[LSKH05] A V Lyamin, S W Sloan, C Krabbenhoft, and M Hjiaj. Lower bound limit analysis with adaptive remeshing. *Int. J. Num. Meth. Engng.*, 63:1961–1974, 2005.

[LZC04] Y Liu, X Zhang, and Z Cen. Numerical determination of limit loads for three-dimensional structures using boundary element method. *Eur. J. Mech. A/Solids*, 23:129–138, 2004.

[MM06] A Makrodimopoulos and C M Martin. Lower bound limit analysis of cohesive-frictional materials using second-order cone programming. *Int. J. Num. Meth. Engng.*, 66:604–634, 2006.

[Pra20] L Prandtl. Über die härte plastischer körper. *Nachrichten von der Gesellshaft der Wissenshaften zu Gottingen Mathematisch-physikalische Klasse*, 9:302–325, 1920.

[SK95] S W Sloan and P W Kleeman. Upper bound limit analysis using discontinuous velocitiy fields. *Comp. Meth. Appl. Mech. Engng.*, 127(5):293–314, 1995.

[Stu99] J F Sturm. Using SeDuMi 1.02, a Matlab toolbox for optimization over symmetric cones. *Optim. Meth. Soft.*, 11-12:625–653, 1999. Avail. http://sedumi.mcmaster.ca.

[TTT03] RH Tütüncü, KC Toh, and MJ Todd. Solving semidefinite-quadratic-linear programs using SDPT3. *Mathem. Progr. Ser. B*, 95:189–217, 2003. Avail. http://www.math.nus.edu.sg/ mattohkc/sdpt3.html.

[ZBS02] N Zouain, L A Borges, and J L Silveira. An algorithm for shakedown analysis with nonlinear yield functions. *Comp. Meth. Appl. Mech. Engng.*, 191:2463–2481, 2002.